

Internal Redox Couple in Silicon-Graphite Anode and its Influence on Degradation of Anode

Junhyuk Moon^{1*+}, Shinya Wakita^{1*}, Heechul Jung^{1*}, Sungnim Cho¹, Jaegu Yoon¹, Joowook Lee¹, Sungsoo Han¹, Sihyung Lee¹, Kimihiko Ito², Yoshimi Kubo², Heung Chan Lee¹⁺, Young-Gyoon Ryu¹⁺

¹Samsung Advanced Institute of Technology, 130 Samsung-ro, Young-gu, Suwon-si, Gyeonggi-do, 16678 Korea

²C4GR-GREEN, National Institute for Materials Science, 1-1 Namiki, Tsukuba, Ibaraki, 305-0044, Japan

*These authors contributed equally to this work.

+Correspondence and requests for materials should be addressed to J.M. (jh.d.moon@samsung.com), H.L. (hchan.lee@samsung.com), and Y.R. (ygyryu@samsung.com).

Recent demands for long range electric vehicles have insisted on high capacity lithium-ion batteries (LiBs) by blending of silicon with graphite. In order to enhance the cell performance, it is important to understand interaction of lithium-ion movements in and between two anode materials with different electrochemical reactions, e.g. formation of Li-Si alloy accompanied with high volume change and intercalation of lithium-ion in graphite during lithiation. Here, we firstly report the methodology for deconvolution of the mixed state in silicon-graphite anode and detailed mechanism on internal redox reaction between silicon and graphite and sequential influence on degradation of silicon-graphite anode. Our results provide an insight to design of materials and an electrode for high performance of a cell.

1. INTRODUCTION

Li-ion batteries have been the predominant power sources for electronic mobile devices for the last two decades, and their applications have widened to other emerging markets, such as electric vehicles (EVs) and energy storage systems (ESSs). Thereby, high energy and high power density lithium-ion (Li^+) batteries are in high demanded and, of course, these require high capacity materials [1]. However, known high capacity materials often have disadvantages on some other properties such as poor cycle performance and safety.

Blending of different active materials can be an effective strategy to balance the merits and demerits of the individual materials, e.g. a blend of LiFePO_4 and $\text{Li}[\text{Li}_{0.17}\text{Mn}_{0.58}\text{Ni}_{0.25}]\text{O}_2$ cathode materials exhibits a balanced performance between energy and power density [2]. Recently, substantial electrochemical interactions between individual materials in blended cathodes during cell operation and their impact on cell performance have been reported [3]. This internal electrochemical

interaction arises from the competition of reaction kinetics and thermodynamic potentials between the individual cathode materials, i.e. internal redox couple [3]. For anodes, the blending of different active materials, e.g. graphite and silicon, is also a well-known strategy to balance silicon's properties, i.e. high capacity but large volume change and pulverization, with that of graphite, i.e. low capacity but structurally stable, to achieve optimized performance [4, 5].

Li-Si alloy has two distinctive material properties. Firstly, the Li^+ mass transport in Si is influenced by the mechano-electrochemical coupling, i.e. the slowing of lithiation by the increased stress in the inner Si particle due to expansion of the lithiated outer layer of the Si particle [6-8]. The Gibbs free energy landscape as a function of lithium compositions is convex in shape, and the ground state phase of Li-Si alloy places near Li_xSi ($x \approx 2.33$) that is the middle of usable maximum Li^+ content in Li_xSi ($x=3.75$) at 1 bar and 298K (ATP) [9, 10]. However, the Gibbs free energy of Li^+ intercalation in graphite continuously decreases until maximum intercalation limit ($x < 1$ in Li_xC_6) [11]. These unique properties can predict the internal redox reaction between silicon and graphite during cycling of a full cell. Secondly, Li-Si alloy has an amorphous phase that is formed during the formation process, a pre-treatment for activation and stabilization of an assembled cell [12]. For this reason, in-operando quantitative analysis of the changing Li-Si phases has been limited despite many studies on in-operando measurements, e.g. Neutron diffraction, X-ray diffraction, and X-ray microscopy [13-16]. In order to improve overall cell performance, e.g. structural and cycling stability, volume changes and electrochemical degradation of anode should be thoroughly understood. Therefore, the mixed state of silicon/graphite anode under non-equilibrium operation conditions should be deconvoluted to the states of each material to reveal the characteristics of the internal redox reaction between silicon and graphite.

Here, we developed a methodology based on in-operando X-ray diffraction (XRD) for deconvolution of the mixed states. This provides us with a quantitative measurement of Li^+ amount in each individual materials, silicon and graphite, during cycling. From the results of the quantitative analysis, we could explain why internal redox reaction in silicon-graphite anode occurs and how these internal redox couples are mechano-electrochemically related for the first time. In addition, their distinctive reaction mechanism during Li^+ insertion and extraction were evaluated based on electrochemical analyses, in-situ thickness measurement, and *ex-situ* soft X-ray absorption fine structure (XAFS). This work also covers a wide range of experimental results with variations of C-rates, size of Si nano-particles (NPs), type of graphites, areal capacity of cells and the blending of anode materials, which enables explication of the detailed mechanisms for lithiation/delithiation as well as degradation of a silicon-graphite anode.

2. EXPERIMENTAL

Preparation of Electrodes: Si/carbon nano-composite (SCN) was prepared as follows: Si nanoparticle was prepared by ball-milling process with micron-sized Si powder followed by chemical vapor deposition to coat carbon on the Si nanoparticle using a custom-made rotary kiln. An additional surface treatment was carried out with coal tar pitch as the carbon source by mixing in a powder mixer and heating at 900 °C for 3h to complete the carbonization reaction. The size of the synthesized SCN particles was in the range of 5 to 15 μm observed by a Scanning Electron Microscope (SEM, Helios NanoLab 450HP, FEI). The specific capacity of SCN was 1460 mAh/g, which was measured using lithium half-cells with the SCN as the working electrode at a delithiation rate of 0.2 C. Here, the areal capacity of electrode was 1.5 mAh/cm². The operation scheme for testing anode material via half cells is constant current-constant voltage (CC-CV) lithiation and constant current (CC) delithiation modes between 1.5 and 0.01V with a 0.05 C cutoff at 25 °C. This measured capacity of SCN was statistically the same as the theoretical capacity of the silicon embedded in the SCN. Hence, capacity portions of the carbon and oxides in SCN could be ignored. The content of silicon in SCN was crosschecked by three different analyses, ion coupled plasma-mass spectroscopy (ICP-MS, ICPS-8100, Shimadzu), thermal gravimetric analysis (TGA, TGA/DSC2, METTLER TOLEDO), and Oxygen Nitrogen Analyzer (EMGA-920, HORIBA).

The anode electrode was fabricated by roll-to-roll coating of slurry dissolved in deionized water on copper foil having 8 μm thickness. The slurries for the areal capacity of 4.4 and 6 mAh/cm² consisted of SCN (14.6 wt%), graphite (82.4 wt%), and binder (3 wt%), and SCN (15.4 wt%), graphite (81.6 wt%), and binder (3 wt%), respectively. Here, we used two types of graphite, Graphite1 and Graphite2. The pellet densities of Graphite1 and Graphite2 were 1.62 g/ml and 1.47 g/ml, respectively. The pellet was fabricated by pressing graphite powder under pressure of 15.4 MPa for 30 seconds. The electrode was dried under vacuum at 130 °C for 3 h and roll-pressed at room temperature in a custom-made line. The specific capacity of the SCN and graphite electrode as the working electrode was 510 mAh/g.

Li_{1.0}Ni_{0.88}Co_{0.08}Mn_{0.04}O₂ Powder (NCM) was prepared by mixing co-precipitated Ni_{0.88}Co_{0.08}Mn_{0.04}(OH)₂ powder with LiOH·H₂O and calcinating the mixture at 750°C for 40 h in O₂ in a custom-made Roller Hearth Kiln (RHK). The washing process involved stirring the prepared NCM powder in deionized water with a mechanical stirrer for 10 min, followed by filtration within 5 min. The weight ratio between the NCM and the washing water was 1:3 (powder/water) over 10 min. The remained water was evaporated in an air convection oven at 720 °C overnight followed heat treatment at 720 °C for 5 h in flowing O₂ gas using RHK. The specific capacity of NCM measured by half cell discharge was 214.8 mAh/g. The operation scheme of the half cell with the cathode material was CC-CV charging and CC discharging modes at 0.2 C between 4.3 and 2.8V with a 0.05 C cutoff at 25 °C.

The cathode electrode was fabricated by roll-to-roll coating of a slurry consisting of NCM (96 wt%), Carbon black (2 wt%, Cabot Co.), and polyvinylidene difluoride (PVDF, 2 wt%, Solef) in N-methyl-2-pyrrolidone (NMP, Sigma-Aldrich) on aluminum foil with 10 μm thickness. The electrode was roll-pressed and dried under vacuum at 120°C in a custom-made line.

Preparation of Cells: Pouch cells of four different electrodes chemistries were tested for in-operando XRD experiments. Hereafter, they will be called as Cell A, B, C and D. Cell A consists of NCM cathode and SCN-graphite1 anode, with the areal capacity of 4.4 mAh/cm². The N/P ratio, capacity ratio between anode and cathode was 1.03. Cell B consists of NCM cathode and Graphite1 anode with 4.4 mAh/cm² and N/P ratio of 1.08, Cell C NCM cathode and SCN-Graphite1 anode with 6 mAh/cm² and 1.03 N/P ratio, and Cell D NCM cathode and SCN-Graphite2 anode with 6 mAh/cm² and 1.03 N/P ratio. The pouch cell composed of two double-side-coated cathodes of 33.4 x 87 mm² size, one double-side-coated anode, and two single-side-coated anodes of 34.4 x 88.5 mm² size separated by a ceramic-coated polyethylene porous film (CCS, Toray). The capacities of Cell A and Cell B were 430mAh, and that of Cell C and Cell D were 630 mAh. All the cells were filled with 1.15 M lithium hexafluorophosphate (LiPF₆, Panax-Etech) dissolved in fluoroethylene carbonate (FEC, Panax-Etech), ethylene carbonate (EC, Panax), ethylmethyl carbonate (EMC, Panax-Etech), and dimethyl carbonate (DMC, Panax-Etech) mixed solvent in 7:7:46:40 by volume, respectively.

For the comparison of size effects of silicon NPs on volume expansion and cyclability, the anodes having the 85 nm and 100 nm silicon NPs (Si 85nm and Si 100nm) embedded in SCNs were tested. The anode electrodes consisted of SCN (14.6 wt%), graphite (82.4 wt%), and binder (3 wt%). For the in-situ thickness measurements, pouch cells were fabricated using the double-side-coated cathode of 32 x 40 mm² size, and the single-side-coated anode of 35 x 85 mm² size which was folded in half length-wise placing the prepared cathode inside with the CCS in-between the cathode and the anode. The cathode powders consisted of Li_{1.0}Ni_{0.6}Co_{0.2}Mn_{0.2}O₂ (80 wt%) and Li_{1.0}Ni_{0.8}Co_{0.1}Al_{0.1}O₂ (20 wt%). These cells were filled with 1.15M LiPF₆ dissolved in EC, EMC, and DMC in 2:4:4 by volume. The areal capacity of these cells was 3.4 mAh/cm² and the N/P ratio was 1.03. Cyclability performance of the anode materials were carried out using so called mini-18650 cells, which are cylindrical-type 18650 cell with a hollowed-out cylindrical PVdF insert to reduce the effective internal cell volume and total capacity of the cell. The mini-18650 cell composed of one double-side-coated cathode of 54 x 200 mm² size and one double-side-coated anode of 57 x 240 mm² separated by the CCS. The cathode powders consisted of Li_{1.0}Ni_{0.6}Co_{0.2}Mn_{0.2}O₂ (80 wt%) and Li_{1.0}Ni_{0.8}Co_{0.1}Al_{0.1}O₂ (20 wt%). These cells were filled with 1.15 M LiPF₆ dissolved in FEC, EC, EMC, and DMC in 7:7:46:40 by volume. The areal capacity and N/P ratio of these cells were 3.4 mAh/cm² and 1.03, respectively.

All cell fabrication, including the electrode coating and assembly of pouch cells, was conducted in a dry room with dew point below -40 °C.

Electrochemical Evaluation: All pouch cells were placed between two aluminum plates under initial pressure of 35 Pa, and were connected with the battery cycle tester (TOSCAT, Toyo). After formation process and two standard cycles, the cells were cycled at 25 °C, with a 10 minutes rest period between cycles. For each cycle, the cells with the areal capacity of 4.4mAh/cm² (Cell A and Cell B) and 6mAh/cm² (Cell C and Cell D) were charged up to 4.3 and 4.25V, respectively at the cycle rates of 1C and 0.5C and held in the constant voltage (CV) charging mode, which was stopped after the charging current was less than 0.05 C. After 10 minute resting period, the cells were discharged down to 2.8V. The large cell performance was characterized using prismatic cell with standard capacity of 8.7 Ah. The electrodes in this prismatic cell were almost the same with those in Cell D, but the silicon NP embedded in SCN in this anode was Si 85nm. The test condition of this cell was identical to that of Cell D.

A three-electrode pouch cell was prepared to characterize the individual electrochemical behavior of the cathode and the anode of a full cell. Lithium foil was placed in the middle of the bottom in order to minimize the over-potential [17]. During cycling, the individual electrode potentials were recorded versus lithium reference electrode.

For the mini-18650 cells, the formation and standard schemes of the cells were 0.1 C and 0.2 C CC-CV charging and CC discharging modes, respectively between 4.2 and 2.8V with a 0.05 C cutoff at 25 °C. The cells were cycled using a 1 C CC-CV charging and CC discharging modes between 4.2 and 2.8V at 25 °C.

Thickness Measurements: In-situ thickness measurements of the single-stack pouch cells during cycling were conducted using a load cell tester. After a 2kg SUS block was imposed on the top of the cells, the cells were connected with the battery cycle tester. The formation and standard schemes of the cells were 0.1 C and 0.2 C CC-CV charging and CC discharging modes, respectively between 4.2 and 2.8V with a 0.05 C cutoff at 25 °C. The cells were cycled using a 0.5 C CC-CV charging and CC discharging modes between 4.2 and 2.8V at 25 °C. The thickness of the cell was monitored with a gap sensor of non-contact displacement measuring system (Linear Gauge System, Mitutoyo) during cycling.

In-Operando XRD: The high x-ray intensity for the operando measurements was achieved with the X-ray diffractometer installed at BL15XU in SPring-8 (Hyogo, Japan). The pouch cell was fully discharged down to 2.8 V with 0.2C rate, and placed between two aluminum plates having beryllium window in the same way described in the electrochemical evaluation section. The photon energy used for transmission through a pouch cell was 18.987 KeV, of which wavelength was 0.65297Å. All diffraction profiles were collected using 4 detectors (1D multichannel) in the range 0 < 2θ < 50°. Sequential XRD profiles were obtained by exposure during 10 seconds every 1 minute for the operation of 1C and 2C rates, and every 2 minutes for the operation of 0.5C rate. The profiles containing the diffraction peaks of graphite and current collector, Cu in the range of 1.45 < q < 2.0 Å⁻¹ were extracted, and were fitted using OriginPro® to

deconvolute and determine the phases of the graphite and their peak intensities. The previous crystallographic data of graphite [18-22] were referred for the fitting. The electrochemical data were measured simultaneously.

XAFS: Ex-situ Si K-edge XAFS was measured at BL-10 in Ritsumeikan SR center. After fully discharging the cell, the cells were disassembled in an Ar-filled glovebox. The anodes were rinsed with DMC for 5 minutes, set on carbon-taped specimen holders, loaded in to an airtight vessel, and then transferred to the BL-10 chamber without exposure to ambient air. The vessel was immediately evacuated, and the specimens were loaded into the measurement chamber with a vacuum level of 5×10^{-8} Pa. The photon beam energy was from 1000 to 2500 eV with a resolution of 0.5 eV or less. The Si K-edge x-ray absorption near edge structure (XANES) of an anode was measured using the total electron yield (TEY, probing depth ~nm) and partial fluorescence yield (PFY, probing depth ~10-10² nm) [23, 24].

Calculation of Lithium-ion Contents in SCN and Graphite: Lithium half-cells with SCN, graphite, and composite of SCN and graphite as a working electrode were composed, respectively. The areal capacity of electrode was 1.5 mAh/cm². Their charge/discharge potentials were measured at 0.05 C, which was presumed to be slow enough to measure pseudo equilibrium potential. Considering the mass ratio of SCN and graphite, the Li⁺ contents in each component in the composite electrode at a certain potential were calculated by using the respectively measured SOC vs. potentials profile of the SCN and graphite. The calculated SOC vs. potential profile for composite electrode was well matched with the measured one. Through this process, the individual SOCs of each material could be separated and simulated in the various compositions.

Image Analysis: The cross sections of anodes were prepared using the ion beam cross section polisher combined with nitrogen cooling system and air isolation system (IB-19520CCP, JEOL), in order to prevent ion-beam damage and exposure to ambient air. These specimens were then transferred to SEM (Helios NanoLab 450HP, FEI) using the air isolation transfer system. The silicon NPs embedded into carbon in SCN were imaged in the Secondary Electron (SE) mode at an accelerating voltage of 2 kV, and magnification at $\times 250000$.

Sets of features corresponding to the Silicon boundaries needed to be extracted from the gray-scaled SEM micrographs. These gray-scaled images were converted to binary images, and the coordinates associated with the boundaries could be estimated. In order to preserve silicon boundaries and edges having large changes in intensity while selectively removing uncertain lines with small intensity fluctuations, L0 gradient minimization [25] (with weighting factor 0.009) was used, which is particularly effective for highlighting silicon boundaries. And morphological processing [26] (dilation / erosion) was used to preserve original object shapes. Otsu's method [27] was used to segment silicon (white, "1") and others (black, "0"). Note that, when silicon was overlapped in the image, silicon particles were partially divided manually. Finally MATLAB[®] 2018a built-in function "regionprops" was conducted to calculate the average particle area and diameter. All algorithms were implemented using MATLAB[®] 2018a (The MathWorks, Inc.).

3. METHODOLOGY: DECONVOLUTION OF MIXED STATE & PRESSURE ON GRAPHITE

After the formation process of cells, their coulomb efficiencies reach as high as over 99.8 %, so we ignore lithium loss due to the solid electrolyte interphase (SEI) formation and the deterioration of electrodes for one cycle. Thus, the Li⁺ amount in only graphite and silicon are considered.

We are able to describe the following linear equation based on the assumption that XRD intensity of each phase is linearly proportional to the lithium content of each phase:

$$\begin{pmatrix} A_i & \cdots & E_i \\ \vdots & \ddots & \vdots \\ A_f & \cdots & E_f \end{pmatrix} \begin{pmatrix} \alpha \\ \vdots \\ \varepsilon \end{pmatrix} + \begin{pmatrix} \varphi_i \\ \vdots \\ \varphi_f \end{pmatrix} = \begin{pmatrix} Capacity_i \\ \vdots \\ Capacity_f \end{pmatrix} \quad \text{Equation. 1}$$

where, A_k , B_k , C_k , D_k , and E_k are intensities of stage1, stage2L, stage2, stage3L, and stage4L, respectively, which are extracted from the fit results of XRD, and α , β , γ , δ , and ε are their coefficients converting the intensity of each phase into its capacity, respectively. φ_k is the Li^+ content in silicon, and Capacity_k is the capacity of a cell in the k^{th} sequential data.

Only the signals from the phase transition of graphite in operando XRD can be detected because the Li-Si alloys are amorphous phases. However, according to Equation (1), the Li^+ amount in silicon can be reconstructed. Firstly, the pseudo-inversion method [28] is applied to the XRD results of the graphite only anode, Cell B, and the coefficients were extracted (Figure 1(a)). The intensities of Cu(111) peaks were used for the normalization of XRD profiles. Then we could calculate Li^+ amount in only graphite in the SCN-graphite composite anode, Cell A, (Figure 1(b)). Finally, we could obtain the Li^+ amount in silicon in the SCN-graphite composite anode of Cell A (Figure 1(c)).

The individual SOCs from XRD of full cell (individual SOCs, circles in Figure 2(a)) and the calculated individual SOCs from electrochemical analysis of half cells (calculated individual SOCs, solid lines in Figure 2(a)) can be compared as shown in Figure 2 (a). Sudden discontinuous changes appear in the individual SOCs of silicon and graphite, marked in red triangles. The appearance of the sudden changes in the data obtained by in-operando XRD is clearer than that in the calculated individual SOCs. These correspond to discontinuities in the potentials at the phase transitions of Li_xSi [29, 30]. Thus, the Li_xSi phase of the shell on silicon particles in the SCN can be determined from previous report [29]. The discrepancy between measured lithium content in silicon and known lithium content at the phase transition of Li_xSi explains that Li^+ insertion into silicon during charging needs high energetic cost that eventually leads to two-phase lithiation [8]. Near the end of charging at SOC 87 %, the large deviation of the individual SOCs from the calculated individual SOCs is a clear signal of the internal redox reaction between silicon and graphite.

The schematic of active material conditions at various SOCs is shown in Figure 2(b), which can be depicted by the analysis of in-operando XRD analysis as previously described. From 2 to 3, Li^+ moves from SCN to graphite as shown in the Figure 1(c). Simultaneously, the pressure applied on the inner of silicon particles might be released, and Li^+ in the shell could also enter into the inner core due to the released pressure. Furthermore, we can estimate the corresponding potential of individual materials, graphite and SCN by aligning individual SOCs in to individual potential as shown in Figure 2(c). During a cycle, the potential of silicon is higher than that of graphite might be due to two-phase lithiation where surface of the silicon particles is highly lithiated. However, the plots in the inset in Figure 2(c), open circuit voltages (OCVs) of graphite (black line) and the shell of silicon particles (red line) show that internal redox reaction is possible. Considering inhomogeneous lithiation of silicon and graphite (only shell of silicon NPs and graphite) to compare with homogeneous lithiation, these plots could be derived from Gibbs free energy of formation of Li_xSi [9, 10], electrochemical potential of Li_yC_6 [11], and the previously described XRD results.

On the other hand, the peaks of LiC_6 (stage 1) in Cell A with composite anode shifting to higher q than that in Cell B with graphite anode were observed as can be seen in Figure 3. The volume expansion of Li_xSi inevitably leads to compression of graphite in the composite anode. From XRD peak shift, the pressure applied on graphite can be calculated using $\Delta P \approx 1/\kappa_c \cdot (c_0 - c)/c_0$. The compressibility of the c axis of LiC_6 is reported to be $\kappa_c = 1/c_0 \cdot (\partial c / \partial P)_{P_0} = 1.344 \times 10^{-2} \text{ GPa}^{-1}$, where c is the c -axis constant and c_0 is the c -axis lattice constant at the reference pressure P_0 [31].

4. RESULTS & DISCUSSION

Why internal redox reaction occurs? The phase of Li_xC_6 could be determined by lithium amount in graphite and the phase of the shell of silicon particles could be also determined using the position of a phase transition from the XRD results. It is hard for Li^+ in the shell on silicon NPs to move into the inner of silicon because of evolved pressure due to volume expansion of the lithiated shell. We can assume that graphite interacts only with the shell of silicon particles. The difference of electrochemical potentials can be described at constant temperature and pressure by the following equation:

$$\Delta\mu = \left(\mu_{\text{Li}_y\text{C}_6} - \mu_{\text{Li}} \right) - \left(\mu_{\text{Li}_x\text{Si}} - \mu_{\text{Li}} \right) = \left(\left. \frac{\partial G_{\text{Li}_y\text{C}_6}}{\partial y} \right|_{T,P} - G_{\text{Li}} \right) - \left(\left. \frac{\partial G_{\text{Li}_x\text{Si}}}{\partial x} \right|_{T,P} - G_{\text{Li}} \right) \quad \text{Equation 2}$$

where $\mu_{\text{Li}_x\text{Si}}$, $\mu_{\text{Li}_y\text{C}_6}$, μ_{Li} , $G_{\text{Li}_x\text{Si}}$, $G_{\text{Li}_y\text{C}_6}$, and G_{Li} are the electrochemical potentials of Li_xSi , Li_yC_6 , and metallic Li and the corresponding Gibbs free energies of formation of Li_xSi , Li_yC_6 , and metallic Li [32] respectively [33]. The electrochemical potential is the change in the corresponding Gibbs free energy that occurs as an amount of lithium changes. In the case of charging Cell A at 0.5 C, 3rd position of a phase transition (red triangle at 65 % SOC) of individual SOCs in Figure 2(a) corresponds to the phase transition from $\text{Li}_{2.3}\text{Si}$ to $\text{Li}_{3.25}\text{Si}$ that is located mostly on the surface of silicon due to the two phase lithiation [29]. The electrochemically active volume, presumably surface, to total volume of the silicon NP can be calculated as 70.7 % from the difference between the surface phase, $\text{Li}_{3.25}\text{Si}$, and the measured total Li^+ content in silicon at 3rd position of a phase transition. With the assumption that the reacted volume will be maintained after 3rd phase transition, the lithiated state of the shell of silicon NPs can be estimated and, subsequently, the electrochemical potentials of $\mu_{\text{Li}_x\text{Si}}$ and $\mu_{\text{Li}_y\text{C}_6}$ can also be calculated using the previously reported thermodynamic values [9, 10, 11]. (Supporting info figures for matching with XRD results) Here, the change in pressure is ignored and the pressure and temperature of this system are set to 1 atm and 297 K. Figure 4 shows the thermodynamic driving force during CV mode and rest. This is the driving force for the internal redox couple. Li^+ can move from silicon to graphite during CV mode. Our situation is different from the conventional solid-solution model for homogenous states, but is well described by Bazant's report for nonequilibrium and inhomogeneous state [34].

In the experiment of a half cell, we could not see internal redox couple. Lithiation in a working electrode is regulated by constant current until set potential, 0.01 V where lithium content in Li_xSi reaches $x=3.75$ [35]. However, lithiation in an anode of a full cell is regulated by the overall potentials difference of cathode and anode. The minimum potential of an anode (~ 0.1 V) during CC mode measured by 3-electrode set up was higher than that measured by a half cell experiment. Therefore, the potential applied on an anode at CV mode was lower than that in half cell.

As shown in Figure 2(a) and Figure 5, the internal redox couple appears in every case. At low C-rate (0.5 C, Figure 2(a)), the individual SOC follows well with the calculated individual SOC. When C-rate increases to 1C and 2C (Figure 5 (a) and (b)), the sudden changes of Li^+ amount are smeared and the individual SOC of silicon becomes lower while that of graphite higher at lower total SOC range than 50%. This might be due to poorer C-rate capability of silicon than that of graphite [36].

What causes an anode to degrade? : As shown in Figure 3, the volume expansion of Li_xSi causes high pressure on graphite. This pressure evolution reduces the spacing of c-axis in graphite. Li-Si alloy itself also shows mechano-electrochemical coupling inside of them. Because Li_xSi has the convex-shaped Gibbs free energy landscape as a function of x in Li_xSi , the favorable phase of Li-Si alloy is $\text{Li}_{2.33}\text{Si}$. The spherical geometry of silicon fundamentally leads to two-phase (de)lithiation. Thus, (de)lithiation in an anode involves a complicated coupling between electrochemical reaction and mechanical stress. Li^+ movements from the shell to the inner of a silicon NP retard by stress evolution during charging. Because of internal redox couple during CV mode, Li^+ in the shell of a silicon NP is moving out, and stress is releasing. Thereby, small amount of Li^+ in the shell could move in the inner of a silicon NP. During discharging, delithiation of the shell of a silicon NP causes the energy and physical barrier for hindering Li^+ move-out in inner of a silicon NP. As a result, once Li^+ moves into the inner of silicon NPs, it is difficult to move out because of the energy landscape of Li-Si alloy and the geometry of silicon. Internal redox couple facilitates Li^+ accumulation in the inner of a silicon NP. Figure 6(a) shows that Li^+ accumulates in the inner of silicon NPs after cycles. When starting a cycle, OCV of the anode at 250th cycle changed to 0.22 V from 0.34 V at 1st cycle, which could be caused by remained lithium of SOC 11 % in the anode. After fully discharging down to 2.8 V at 0.2 C before XRD measurements, Li^+ amount in graphite is 8.1 mAh. However, Li^+ amount remained in silicon and graphite at the end of the discharge (blue triangle in Figure 6 (a)) are 19 and 5.1 mAh, respectively, and this remained Li^+ amount is 3.7 % of charging capacity. While Li^+ amount in silicon smoothly increases at 1st cycle during the charge from -400 mAh to -200 mAh (red closed circles in Figure 6 (a)), Li^+ amount in silicon at 250th cycle (red open circles in Figure 6 (a)) increases with the same slope of that at 1st cycle until the begin of plateau (from $x=0$ to 1 in Li_xSi), and at the end of plateau, Li^+ amount in silicon begins to increase with the same slope of that at 1st cycle again (from $x=1.3$ to 1.7 in Li_xSi). In the plateau (black line on red open circles in Figure 6(a)), Li^+ could not be inserted into silicon NPs because of the accumulated Li^+ in the inner of silicon NPs.

Li^+ accumulating in silicon might cause mechanical stress on the outside shell of the silicon NPs. Consequently, the degradation of silicon-surface could be accelerated, and the available region which Li^+ can be inserted in silicon is reduced. In graphite, the pressure onto graphite becomes also larger due to expansion of silicon in which Li^+ is accumulated during cycles. This pressure hinders the Li^+ movement in graphite, especially the transition from stage 2 (LiC_{12}) to stage 1 (LiC_6) as shown in Figure 6(b). Li^+ amount in stage 1 at 1st cycle (gray circles in Figure 6(b)) becomes larger than that at 250th cycle (black open circles in Figure 6(b)) while Li^+ amount in stage 2 at 1st cycle becomes smaller than that at 250th cycle from -200 to -100 mAh. Because of physical and chemical degradations in anode materials and volume expansion of silicon NPs, the anode materials would feel the larger current density, and the porosity in the anode electrode would change dramatically during a cycle and decrease after cycles [37]. This probably induces the deposition of lithium and accelerates to degrade a cell. Additionally, the internal redox reaction leads to increase the potential of anode because of delithiation of Li_xSi during CV mode. Consequently the time for CV mode should be increased. Cathode materials have got to suffer from delithiated state at high cut-off voltage during CV mode.

Our finding provides new perspectives on design of materials and electrode. First, we have to use graphite having low energy barrier for the transition from stage2 (LiC_{12}) to stage1 (LiC_6) under high pressure (~0.4GPa). Second, we have to reduce the Li^+ amount accumulating in the inner of silicon NPs. The pressure on graphite evolves during charge as shown in Figure 7(a). At that time, Li^+ amount in stage 2 of Cell C is larger than that of Cell D in Figure 7(b). That means that the transition from stage2 to stage1 in Cell D is easier than that in Cell C under high pressure on graphite. On the basis of our finding, the size of a silicon NP is reduced to 85 nm of its long-axis in order to enhance homogeneity of reaction in a silicon NP, and their performance are compared with that of Si 100 nm as shown in Figure 8. When the size of silicon NPs decreases, the electrochemical reaction could be homogeneous in a silicon NP and the Li^+ accumulation could be reduced, i.e. the reduction of its size decreases not only accumulation of Li^+ in silicon NPs but also degradation of materials. The thickness evolutions as shown in Figure 8(c), the capacity retentions in Figure 8(d) and the peak evolutions of lithium silicate and silicon oxide in XANES (Figure 9 (a) and (c)) dovetail with this hypothesis. Figure 10 shows the cycling performance of the prismatic cell using improved materials, Graphite2 and Si 85nm. This cell exhibits good performance with capacity retention over 80% after 750 cycles.

The anode electrode have designed on the assumption that the phase of Li_xSi would be $x=3.75$ at full lithiation. However, the phase of $\text{Li}_{3.75}\text{Si}$ cannot be reached in the operation of a full cell because of internal redox couple. The conventional design of electrode induces the internal redox couple and this internal redox couple facilitates degradation of a cell. Thereby, the design of anode electrode changed in order to reduce the internal redox reaction. In the new design, the content of graphite was fixed, and the content of SCN was 110% higher than that in the previous design. New anode electrode consisted of SCN (18 wt%),

Graphite2 (79 wt%), and binder (3 wt%). In this design, the cross point of individual SOC of SCN and graphite is higher SOC than that in the previous design as shown in Figure 11(a). For this reason, we can estimate the status of a cell as following. When adding 10 % SCN in the anode electrode, the reduction of internal redox reaction could lead to reduced time for CV mode as well as enhanced cycle retention. Moreover, whenever the design of an anode is changed, the potential of an anode during CV mode would be almost unchanged because of internal redox couple. Our expectation agrees well with experimental results such as the cycle retention, the ratio of the time for CV mode to the total charging time (Figure 11(b)), and the individual potentials at the end of charging (Figure 11 (c) and (d)).

5. CONCLUSION

In summary, we deconvolute the mixed state in silicon-graphite anode with the phases and potentials of individual material during a cycle. We can thereby measure Li^+ mass transport of individual materials quantitatively.

Our work finds and sheds light on the internal redox reaction between silicon and graphite, and the complicated coupling between electrochemical reaction and mechanical stress for the first time. The reversal of the difference of the electrochemical potentials between Li_xSi and Li_xC_6 drives the Li^+ mass transport from silicon to graphite during CV mode (internal redox couple). The internal redox couple would induce small amount of Li^+ to move in the inner of a silicon NP at the end of charge. Sequentially, the energy barrier and the inhomogeneity of reaction in a silicon NP leads to Li^+ accumulation in the inner of a silicon NP during discharging process. Due to this Li^+ accumulation, the evolution of pressure on graphite suppresses the Li^+ intercalation into graphite (coupling between reaction and stress).

Based on the detailed mechanism, we show that new design of materials and an electrode have to be required for high performance of a cell. Our work provides new perspectives on the blending of silicon and graphite.

REFERENCES AND NOTES

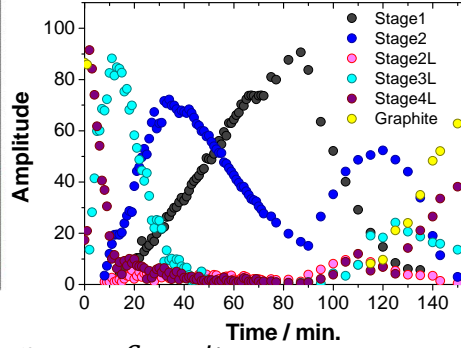
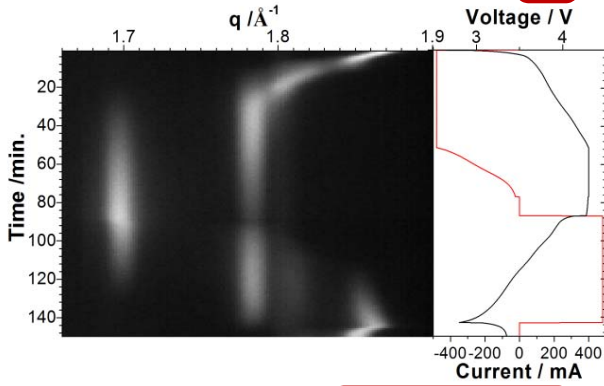
- [1] Chan, C. K. et al. High-Performance Lithium Battery Anodes Using Silicon Nanowires. *Nature Nanotechnology* **3**, 31– 35 (2008)
- [2] Whitacre, J. F. et al. Dual active material composite cathode structures for Li-ion batteries. *Journal of Power Sources* **177**, 528-536 (2008)
- [3] Heubner, C. et al. Recent insights into the electrochemical behavior of blended lithium insertion cathodes: A review. *Electrochimica Acta* **269**, 745-760 (2018)
- [4] Zhou, M. et al. Anisotropic Interfacial Friction of Inclined Multiwall Carbon Nanotube Array Surface. *Carbon*, **50**, 5372– 5379 (2012)
- [5] Liu, N. et al. A Pomegranate-Inspired Nanoscale Design for Large-Volume-Change Lithium Battery Anodes. *Nature Nanotechnology* **9**, 187– 192 (2014)
- [6] Zhang, X. et al. A reaction-controlled diffusion model for the lithiation of silicon in lithium-ion batteries. *Extreme Mechanics Letters* **4**, 61-75 (2015)
- [7] Liu, X. H. et al. Self-Limiting Lithiation in Silicon Nanowires. *ACS Nano* **7**, 1495-1503 (2013)

- [8] Wang, J. W. et al. Two-Phase Electrochemical Lithiation in Amorphous Silicon. *Nano Letters* **13**, 709-715 (2013)
- [9] Tipton, W. W. et al. Structures, phase stabilities, and electrical potentials of Li-Si battery anode materials. *Physical Review B* **87**, 184114 (2013)
- [10] Liang, S.-M. et al. Thermodynamics of Li-Si and Li-Si-H phase diagrams applied to hydrogen absorption and Li-ion batteries. *Intermetallics* **81**, 32-46 (2017)
- [11] Reynier, Y. et al. The entropy and enthalpy of lithium intercalation into graphite. *Journal of Power Sources* **119-121**, 850-855 (2003)
- [12] Li, J. and Dahn, J. R. An in situ X-ray diffraction study of the reaction of Li with crystalline Si. *Journal of The Electrochemical Society* **154**, A156-A161 (2007)
- [13] Wang, X.-L. et al. Visualizing the chemistry and structure dynamics in lithium-ion batteries by in-situ neutron diffraction. *Scientific Reports* **2**, 747 (2012)
- [14] Pietsch, P. et al. Combining operando synchrotron X-ray tomographic microscopy and scanning X-ray diffraction to study lithium ion batteries. *Scientific Reports* **6**, 27994 (2016)
- [15] Taminato, S. et al. Real-time observations of lithium battery reactions-operando neutron diffraction analysis during practical operation. *Scientific Reports* **6**, 28843 (2016)
- [16] Pietsch, P. et al. Quantifying microstructural dynamics and electrochemical activity of graphite and silicon-graphite lithium ion battery anodes. *Nature Communications* **7**, 12909 (2016)
- [17] Mitsuda, K., Hara, S., Takemura, D. Polarization Study and AC-Impedance Measurement in the Horizontal Plane of a Lithium-ion Battery Using Eight Reference Electrodes. *Electrochemistry* **84**, 861-871 (2016)
- [18] Ohzuku, T., Iwakoshi, Y., Sawai, K. Formation of Lithium-Graphite Intercalation Compounds in Nonaqueous Electrolytes and Their Application as a Negative Electrode for a Lithium Ion (Shuttlecock) Cell. *Journal of the Electrochemical Society* **140**, 2490-2498 (1993)
- [19] Billaud, D., Henry, F. X. Structural studies of the stage III lithium graphite intercalation compound. *Solid State Communications* **124**, 299-304 (2002)
- [20] Billaud, D., Henry, F. X., Lelaurain, M., Willmann, P. Revisited Structures of Dense and Dilute Stage II Lithium-Graphite Intercalation Compounds. *Journal of Physics and Chemistry of Solids* **57**, 775-781 (1996)
- [21] Woo, K. C. et al. Effect of In-Plane Density on the Structural and Elastic Properties of Graphite Intercalation Compounds. *Physical Review Letters* **50**, 182-185 (1983)
- [22] Guerard, D., Herold, A. Intercalation of lithium into graphite and other carbons. *Carbon* **13**, 337-345 (1975)
- [23] Jiang, D. T. et al. Observations on the surface and bulk luminescence of porous silicon. *Journal of Applied Physics* **74**, 6335 (1993)
- [24] Sham, T. K. et al. Electronic structure and optical properties of silicon nanowires: A study using x-ray excited optical luminescence and x-ray emission spectroscopy. *Physical Review B* **70**, 045313 (2004)
- [25] Xu, L., Lu, C., Xu, Y., Jia, K. Image smoothing via L0 gradient minimization. *ACM Transactions on Graphics* **30**, 174-184 (2011)
- [26] Serra, J. Image Analysis and Mathematical Morphology, vol. 1. London: *Academic Press*, 1982

- [27] Otsu, N. A threshold selection method from gray-level histograms. *IEEE Transactions on Systems, Man, and Cybernetic* **SMC-9**, 62–66 (1979)
- [28] Penrose, R. On best approximate solution of linear matrix equations. *Proceedings of the Cambridge Philosophical Society* **52**, 17-19 (1956)
- [29] Wen, C. J. and Huggins, R. A. Chemical Diffusion in Intermediate Phases in the Lithium-Silicon System. *Journal of Solid State Chemistry* **37**, 271-278 (1981)
- [30] The potential of silicon (E) versus the amount of Li (n) near phase transition point (E^*) have the form such as $-u(x)$, where $u(x)$ is the step function, so that asymptotic form of n versus E is $\tanh^{-1}x$. The average number of Li in Li-Si alloy is $\langle n \rangle = -\partial G / \partial \mu \propto \partial(nE) / \partial E|_{E \approx E^*} \sim d \tanh^{-1} E / dE|_{E \approx E^*} = 1/(1 - E^2)|_{E \approx E^*}$. When phase transition of silicon occurs, the change in Li number in Li-Si alloy can be so sudden.
- [31] Kganyago, K.R. et al. Structural and electronic properties of lithium intercalated graphite LiC_6 . *Physical Review B* **68**, 205111 (2003)
- [32] Barin I., Platzki G. Thermochemical data of pure substances, 3rd ed. New York: VCH: Weinheim, 1995
- [33] Aydinol M. K. et al. Ab initio study of lithium intercalation in metal oxides and metal dichalcogenides. *Physical Review B* **56**, 1354-1365 (1997)
- [34] Bazant, M. Z. Theory of Chemical Kinetics and Charge Transfer based on Nonequilibrium Thermodynamics. *Accounts of Chemical Research* **46**, 1144-1160 (2013)
- [35] Hatchard, T. D. and Dahn, J. R. In Situ XRD and Electrochemical Study of the Reaction of Lithium with Amorphous Silicon. *Journal of The Electrochemical Society* **151**, A838-A842 (2004)
- [36] Su, X. et al. Silicon-Based Nanomaterials for Lithium-ion Batteries: A Review. *Advanced Energy Materials* **4**, 1300882 (2014)
- [37] Radvanyi, E. et al. Failure mechanisms of nano-silicon anodes upon cycling: an electrode porosity evolution model. *Physical Chemistry Chemical Physics* **16**, 17142 (2014)
- [38] Yamada, M. et al. Reaction Mechanism of "SiO"-Carbon Composite-Negative Electrode for High-Capacity Lithium-Ion Batteries. *Journal of the Electrochemical Society* **159**, A1630-A1635 (2012)
- [39] Schroder, K. et al. The Effect of Fluoroethylene Carbonate as an Additive on the Solid Electrolyte Interphase on Silicon Lithium-Ion Electrodes. *Chemistry of Materials* **27**, 5531 (2015)
- [40] Sina, M. et al. Direct Visualization of the Solid Electrolyte Interphase and Its Effects on Silicon Electrochemical Performance. *Advanced Materials Interfaces* **3**, 1600438 (2016)

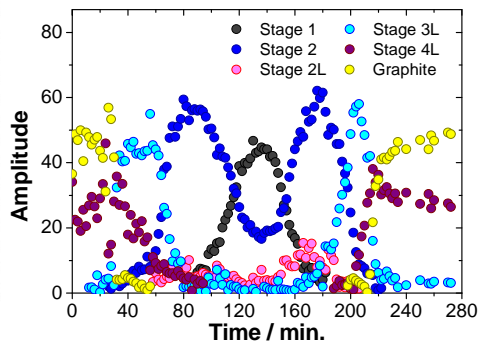
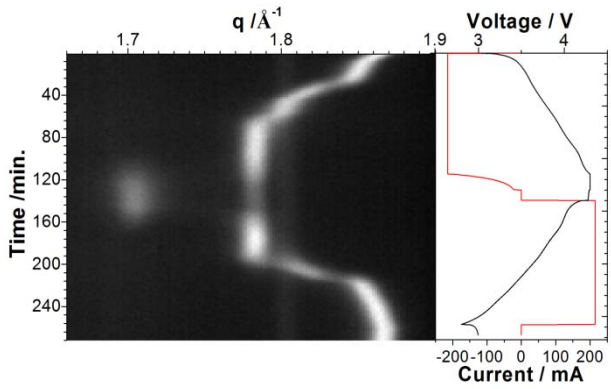
(a) Graphite

$$\begin{pmatrix} A_i & \cdots & E_i \\ \vdots & \ddots & \vdots \\ A_f & \cdots & E_f \end{pmatrix} \begin{pmatrix} \alpha \\ \vdots \\ \varepsilon \end{pmatrix} + \begin{pmatrix} \varphi_i \\ \vdots \\ \varphi_f \end{pmatrix} = \begin{pmatrix} Capacity_i \\ \vdots \\ Capacity_f \end{pmatrix}$$



(b) SCN-Graphite

$$\begin{pmatrix} A_i & \cdots & E_i \\ \vdots & \ddots & \vdots \\ A_f & \cdots & E_f \end{pmatrix} \begin{pmatrix} \alpha \\ \vdots \\ \varepsilon \end{pmatrix} + \begin{pmatrix} \varphi_i \\ \vdots \\ \varphi_f \end{pmatrix} = \begin{pmatrix} Capacity_i \\ \vdots \\ Capacity_f \end{pmatrix}$$



(c)

$$\begin{pmatrix} A_i & \cdots & E_i \\ \vdots & \ddots & \vdots \\ A_f & \cdots & E_f \end{pmatrix} \begin{pmatrix} \alpha \\ \vdots \\ \varepsilon \end{pmatrix} + \begin{pmatrix} \varphi_i \\ \vdots \\ \varphi_f \end{pmatrix} = \begin{pmatrix} \text{Capacity}_i \\ \vdots \\ \text{Capacity}_f \end{pmatrix}$$

In Graphite In SCN

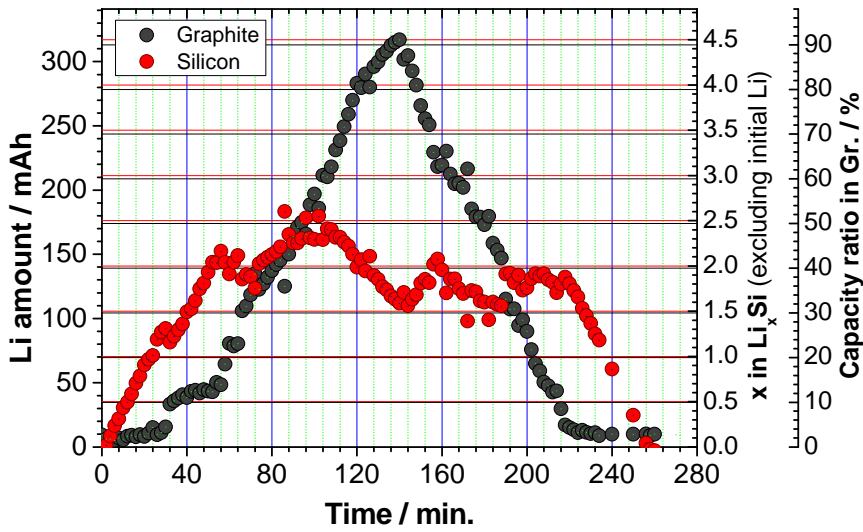


Figure. 1. The methodology for deconvolution of mixed state

(a) and (b) are X-ray diffraction profiles of anodes and the corresponding voltage and current profiles during battery operation. The amplitude profiles of the stages of graphite in an anode after refinement process are indicated on the right of each XRD corresponding with voltage and current profile. The coefficients for converting the amplitude of each stage to its capacity were obtained from data of Cell B using pseudo-inversion method. The amplitude profiles of the stages of graphite in Cell A were converted to their profiles of Li^+ amount using the calculated coefficients. Sequentially, the profile of Li^+ amount in silicon could be obtained. (c) The mixed state in the anode of Cell A at 0.5 C could be deconvoluted with silicon and graphite. Two left y-axes, x in Li_xSi (red lines) and capacity ratio (black lines) in graphite, indicate ancillary information on the averaged Li^+ numbers per a silicon atom and the SOC in graphite.

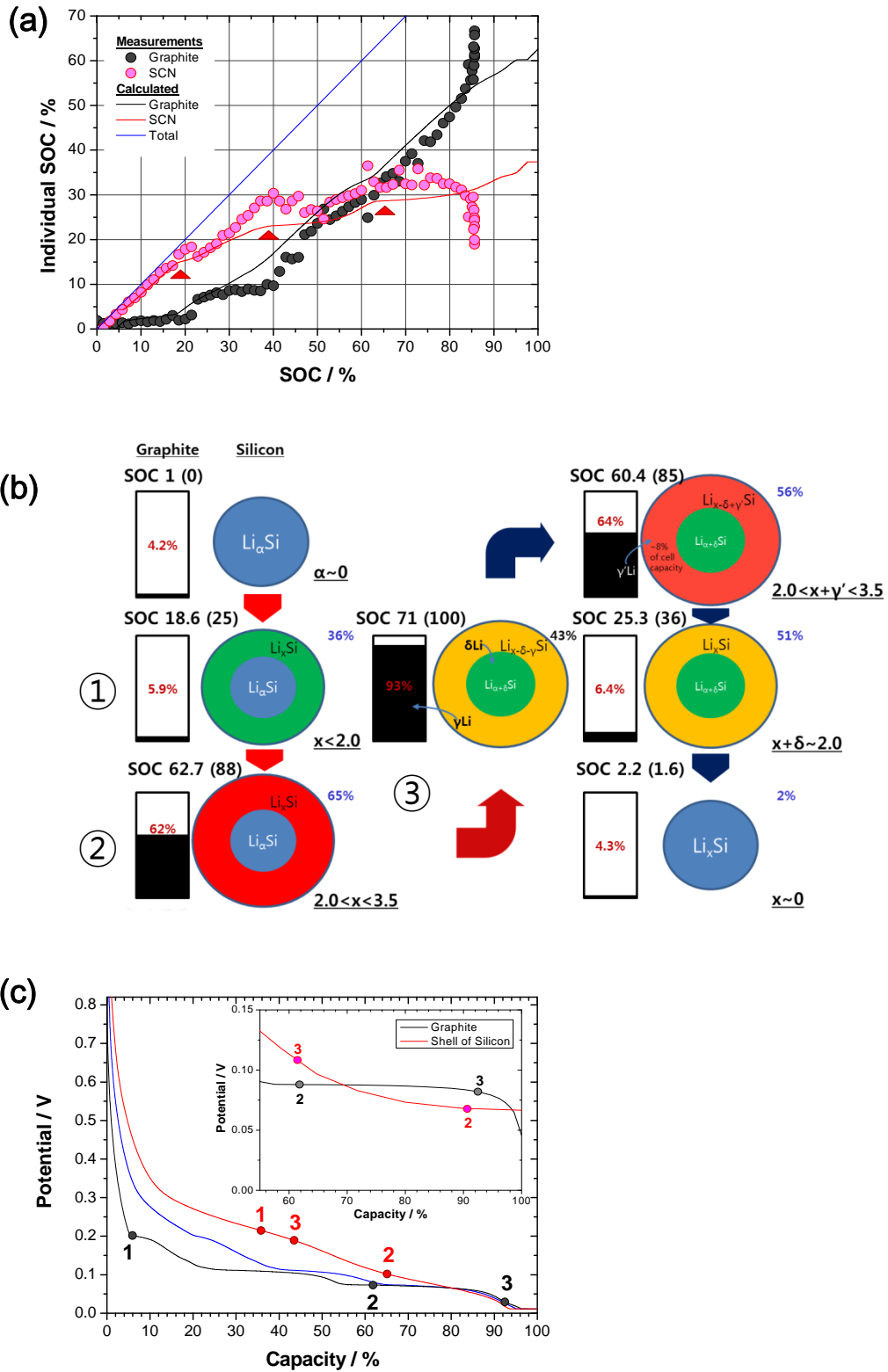


Figure 2. The individual SOCs, the schematic of the SOCs in individual material, silicon and graphite, and the structural change of a silicon particle, and the corresponding potentials during 1st charge and discharge processes of Cell A at 0.5 C

Plots (a) are the SOC in individual material, SCN and graphite, during charging at 0.5 C. The reaction barriers (sudden changes of Li^+ amount in the individual SOC of Li_xSi) appear in the calculated individual SOC (red triangles) and the experimental data and the appearance of sudden changes of Li^+ amount is typical for Li_xSi phase transformation. Near the end of charge, experimental data gotten from full cells distinctly deviate from the calculated individual SOC obtained from a half cell. These obviously indicate the internal redox reaction between graphite and SCN. The discrepancy between the ends of SOC originates from the utilization of active materials and the N/P ratio. (b) The schematic of Li^+ amount in a silicon particle and graphite is able to be described by the analysis of XRD data during a cycle at 0.5 C. SOC in schematic is SOC of anode and the number in brackets is SOC of cell. The corresponding SOC of graphite and silicon are indicated as red and blue number, respectively. Herein, the phases of Li_xSi were estimated using dQ/dV curve derived from the potential of anode by 3-electrode analysis. The large volume expansion during insertion of Li^+ into Si causes the two-phase lithiation. The formation energy of Li_xSi and the geometry of silicon NPs lead to the two-phase delithiation. (c) The black and red circles are the corresponding potentials of individual materials, graphite and silicon. During a cycle, the potential of silicon is higher than that of graphite due to two-phase lithiation. However, plots in the inset, open circuit voltages of graphite (black line) and the shell of silicon particles (red line) show that internal redox reaction is possible. These plots could be derived from Gibbs free energy of formation of Li_xSi and XRD results. Our methodology provides us quantitative information on state and potential of individual material in silicon-graphite anode as described earlier.

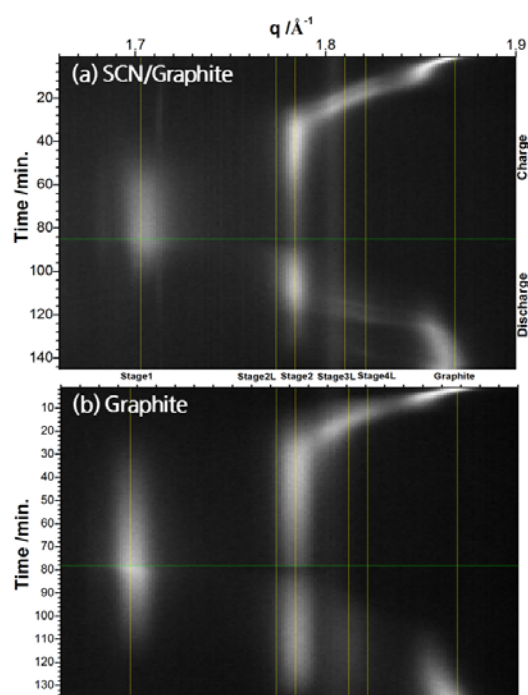


Figure 3. Pressure applied on graphite

The peak positions of LiC_6 (stage 1) in Cell A (a) are shifting to higher position than that in Cell B (b). This peak shift indicates that graphite is under high pressure by large volume expansion during insertion of Li into Si.

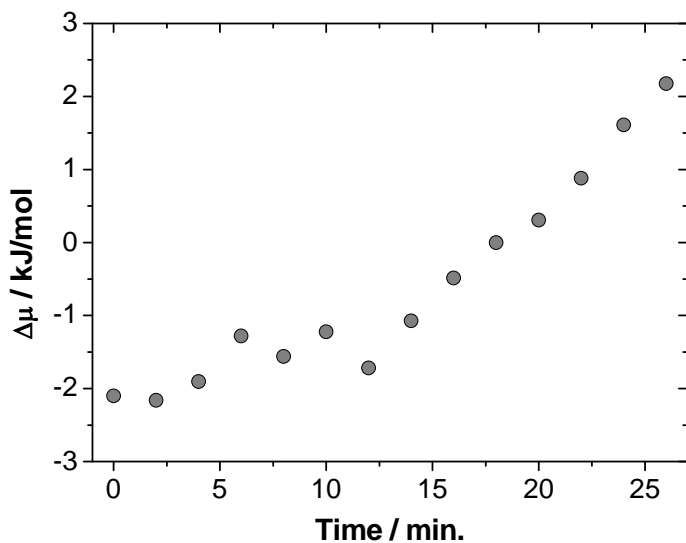


Figure 4. The thermodynamic driving force during CV mode and rest time of Cell A at 0.5 C

The start time of CV mode is set to 0 minute. After 17 minutes, the cell is in rest. The difference of electrochemical potentials between Li_xC_6 and Li_xSi becomes decreasing because of the internal redox couple between silicon and graphite. Because of inhomogeneous and non-equilibrium reaction, the over-reaction in rest would occur.

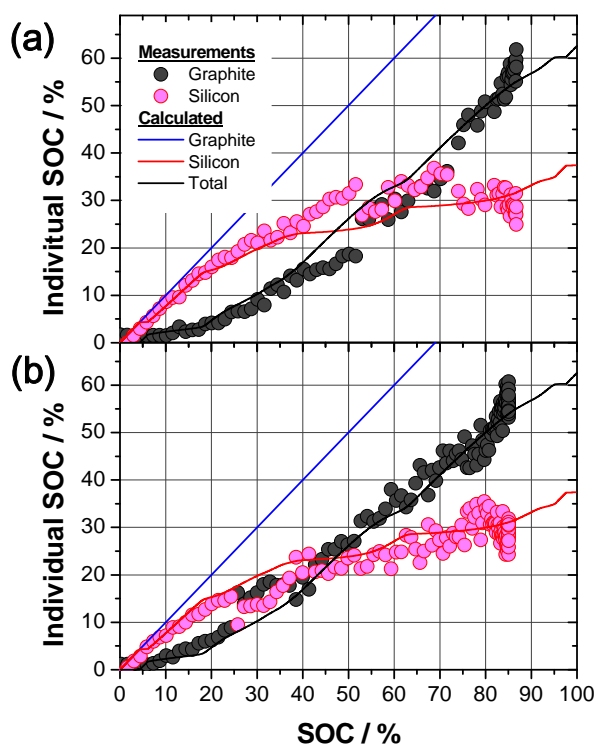
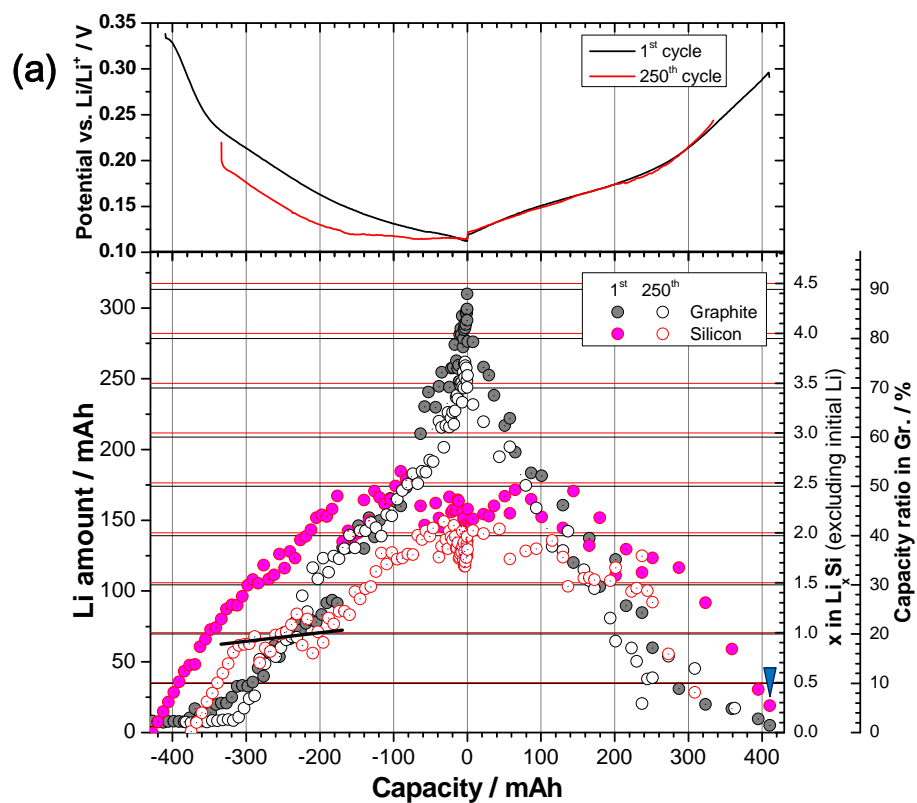


Figure 5. The SOC in individual material during charging at 1 C and 2 C

(a) and (b) are comparisons between the individual SOC and the calculated individual SOC in the anode of Cell A during a charge process at 1 C and 2 C, respectively. The lines were drawn based on the experiments of half cells at low rates. The red and black circles were obtained by experiments of full cells.



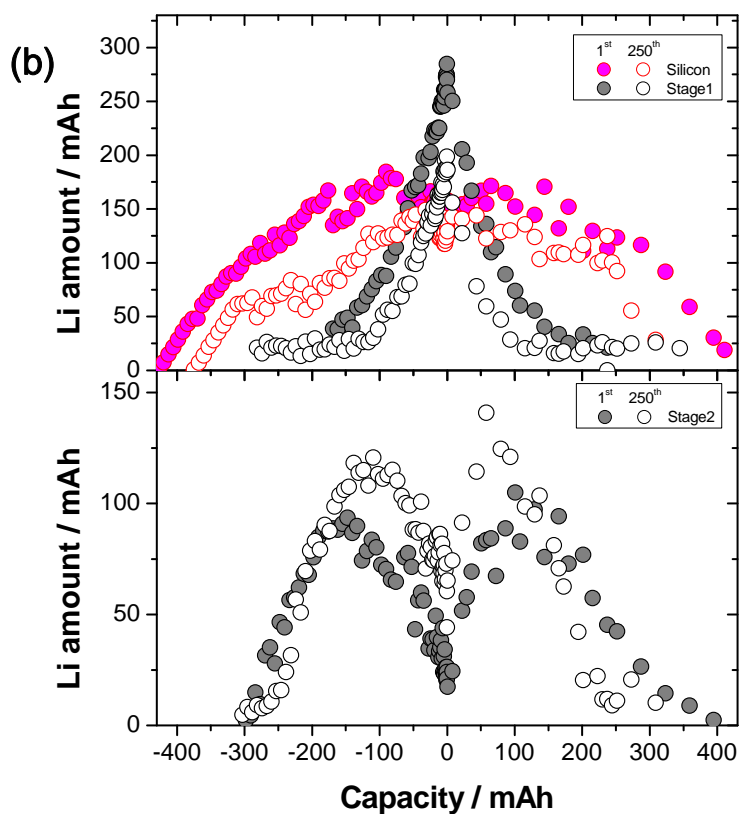


Figure 6. Comparison of the lithium movements between the 1st cycle and the 250th cycle of Cell A

The upper graph of (a) is the potential of anode, which is obtained by the 3-electrodes cell measurements. When starting of a cycle, OCV of 250th cycle is lower than that of 1st cycle. With cycles, Li⁺ accumulates in the anode, especially silicon. In the lower graph of (a), the slopes from $x=0$ to 1 and from $x=1.3$ to 1.7 in Li_xSi on the lithium amount in silicon at 250th cycle are the same with that of lithium amount in silicon at 1st cycle, In the plateau (black line on red open circles in Figure 6(a)), Li⁺ could not be inserted into silicon NPs because of the accumulated Li⁺ in the inner of silicon NPs. This imply that the accumulation of Li⁺ in the inner of silicon NPs. At the end of discharging, Li⁺ in silicon cannot fully move out (blue triangles). This also supports our hypothesis about the lithium accumulation. Plots of (b) show that the expansion of a Li-Si alloy due to accumulation of Li⁺ in the inner of silicon NPs hinders the transition from stage 2 (LiC_{12}) to stage 1 (LiC_6).

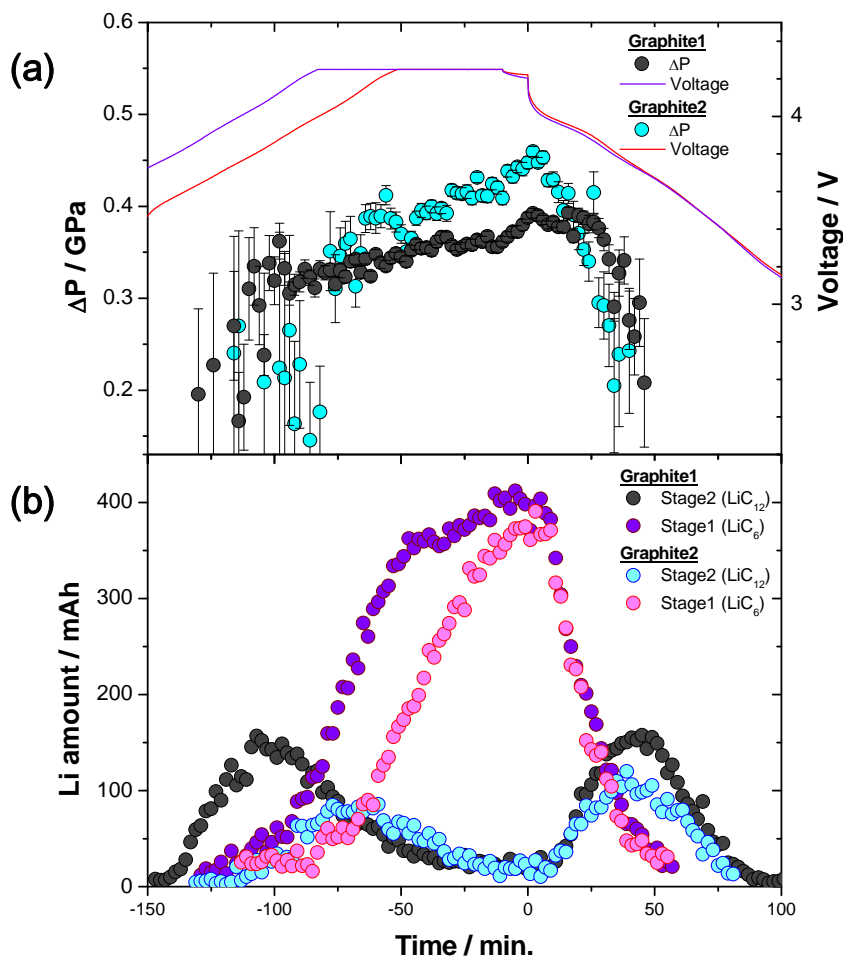
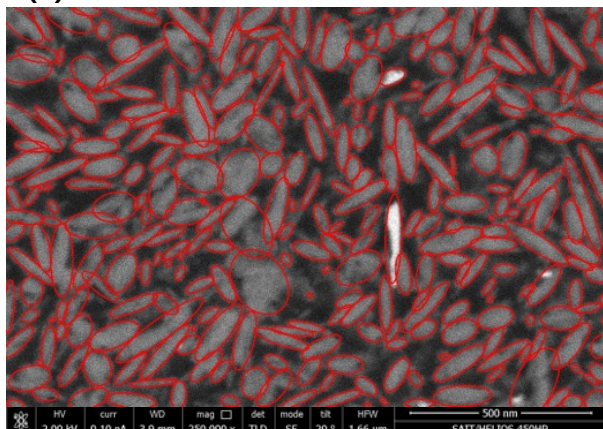
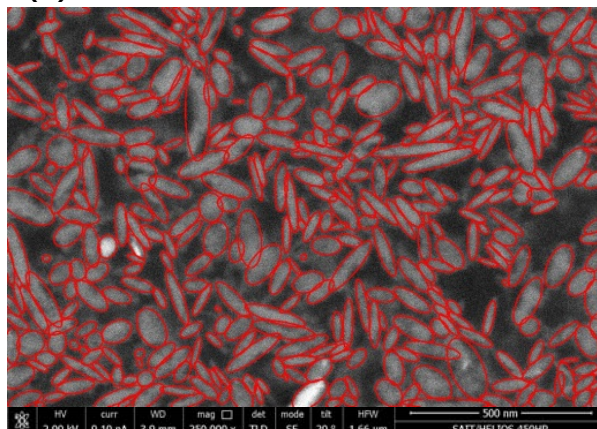
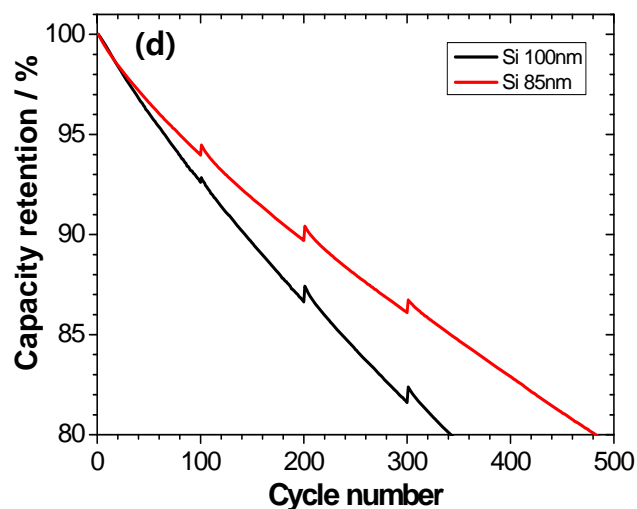
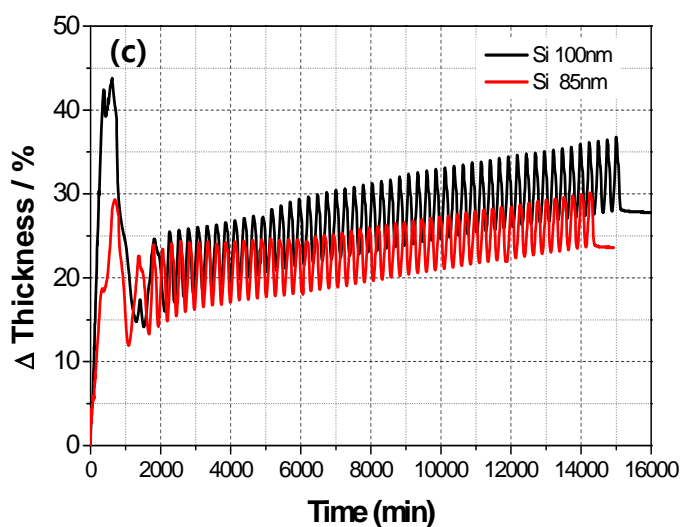


Figure 7. Evolution of pressure on graphite and Li movement in graphite under high pressure by the volume expansion of Li_xSi and the sequent Li intercalation into graphite

For comparison of Cell C with Cell D, the start time of discharge is set to 0 minute. (a) The pressure on graphite evolves by the expansion of Li_xSi and the sequent Li^+ intercalation into graphite. (b) During charging, the maximum Li^+ amount in stage2 in Cell C is larger than that in Cell D. This indicates that the transition from stage2 (LiC_{12}) to stage1 (LiC_6) in Cell C is energetically more difficult than that in Cell D.

(a) Si 100nm**(b) Si 85nm**

	Avg. length of long axis	Avg. length of short axis	Equivalent radius
Si 100nm	99.905nm	37.76nm	27.608nm
Si 85nm	85.604nm	33.246nm	24.213nm

**Figure 8. Size effect of a silicon NP on the cell expansion.**

The SCN is composed of silicon NP embedded into carbon. (a) and (b) are SEM micrographs of their sections. The boundaries of silicon NP are marked by red lines. The table below indicates the averaged lengths of long axes, short axes and the equivalent radii obtained from SEM micrographs. The smaller the size of silicon NP becomes, the smaller the accumulated lithium in the inner of silicon NP. Consequently, the cell expansion is reduced after cycling. (c) the expansion of the cell using Si 85nm is lower than that of the cell using Si 100nm. Furthermore, expanding of silicon by Li^+ accumulating in its inner core leads mechanical stress on the outer of silicon particles. This accelerates the chemical degradation of silicon-surface, and the physical degradation of graphite due to silicon expansion. (d) the cell with Si 85nm has better performance than that with Si 100nm.

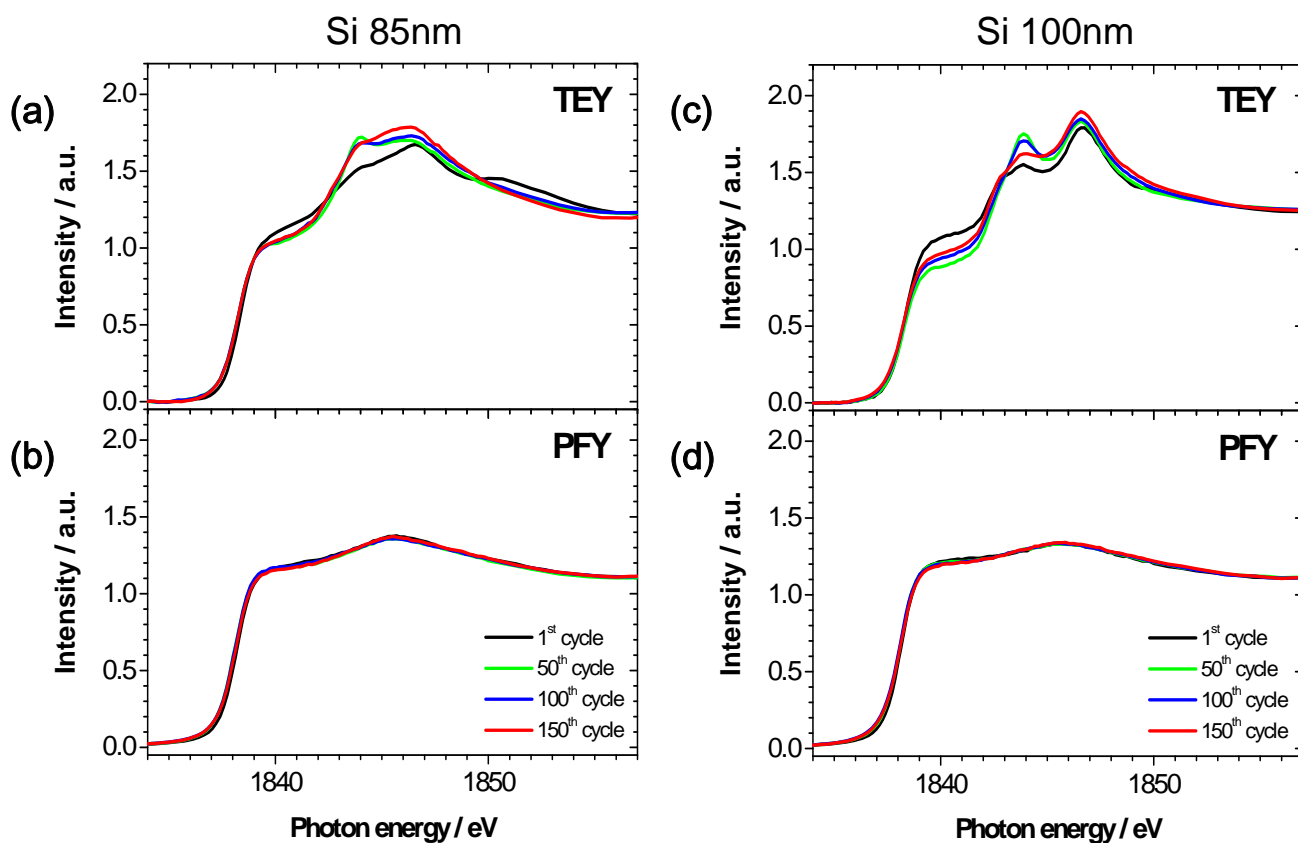


Figure 9. Size effect of a silicon NP on degradation of silicon.

The increase of peaks at 1843 and 1847 eV indicates the evolution of lithium silicate (Li_xSiO_y) and silicon oxide (SiO_x) respectively which lead to the high impedance and low specific capacity retention [38-40]. The TEY XANES strongly support that (a) the surface degradation of silicon particles in the cell using Si 85nm is less than (c) that in the cell using Si 100nm after cycles. (b), (d) The PFY XANES show that the bulk properties of silicon particles almost do not change after cycles.

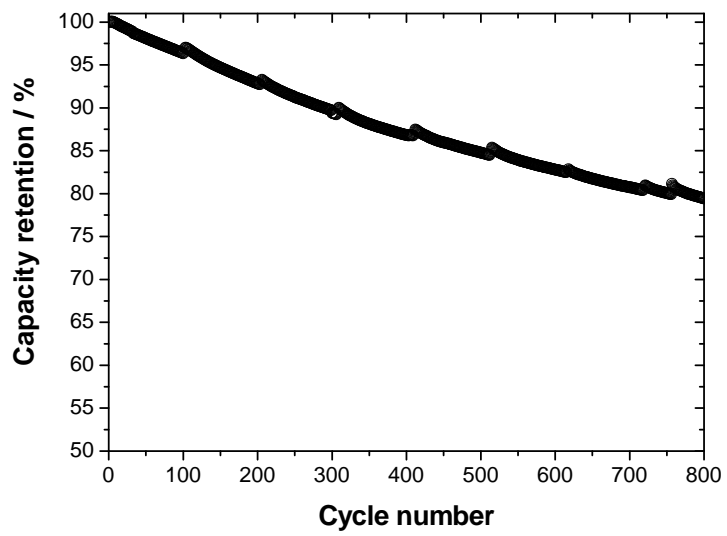


Figure 10. The cycling performance of the prismatic cell with capacity of 8.7 Ah.

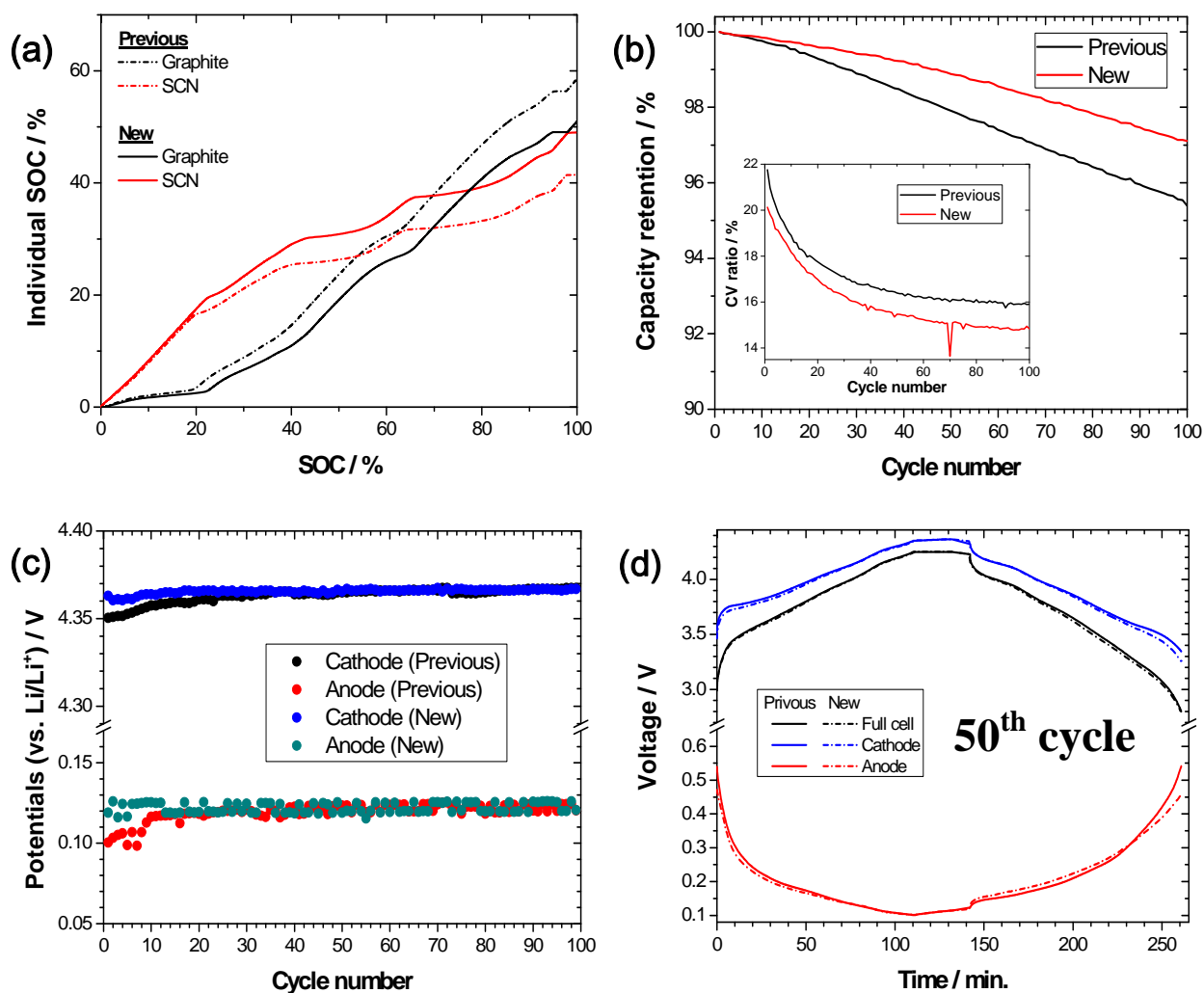
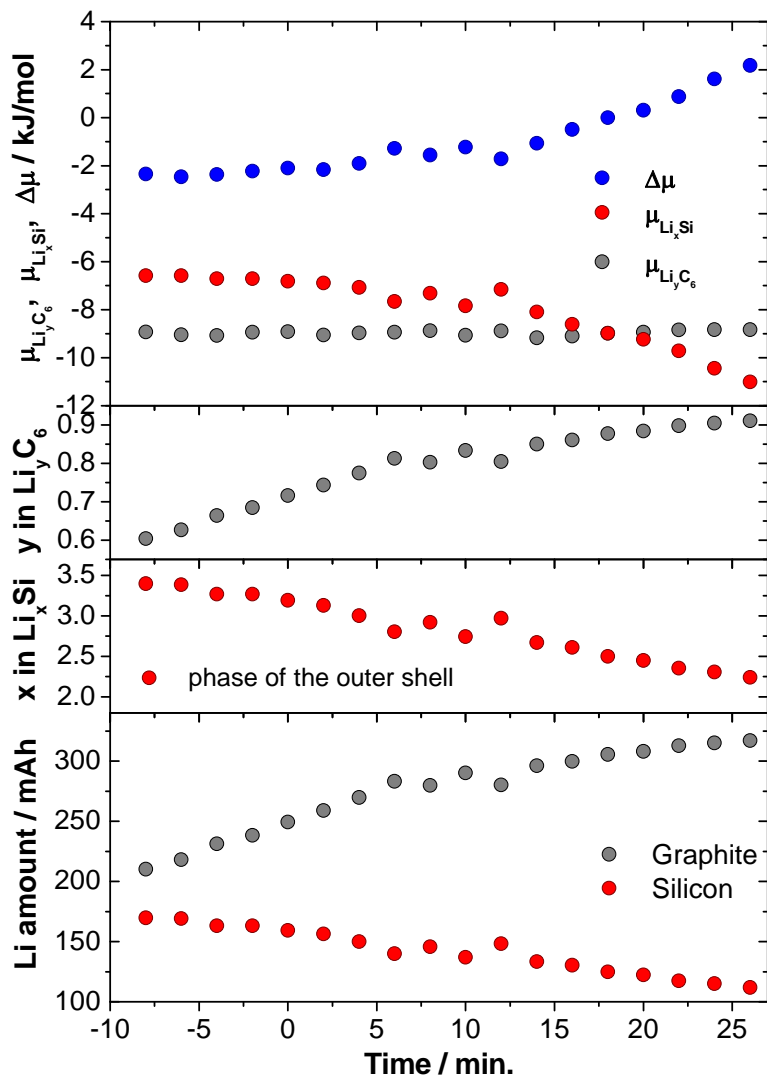


Figure 11. Change of the design of electrode.

The graph (a) is the comparison of the calculated individual SOC between previous and new design. In new design, the cross point of individual SOC of SCN and graphite is higher SOC than that in the previous design, i.e. new design can reduce the internal redox reaction. The performance of the cell having newly designed anode electrode is compared with that of the previous cell. New cell show the higher performance such as (b) capacity retention and ratio of the time for CV mode to total charging time (CV ratio). The graph shown in (c) is the individual potentials of a cathode and an anode at the end of charge and at the start of discharge respectively every a cycle. The potential profiles shown in (d) are the potential of full cell and the individual electrode potentials at 50th cycle.



Supporting info figures for matching with XRD results during CV mode and rest time of Cell A at 0.5 C

The start time of CV mode is set to 0 minute. After 17 minutes, the cell is in rest.